

Linear analysis of the vertical shear instability: outstanding issues and improved solutions (Research Note)

O. M. Umurhan^{1,2}, R. P. Nelson³ and O. Gressel⁴

¹ Space Sciences Division, NASA Ames Research Center, Moffett Field, CA 94035.

² SETI Institute, 189 Bernardo Way, Mountain View CA 94043, USA

³ Queen Mary University of London, School of Physics and Astronomy, 327 Mile End Road London, E1 4NS, UK

⁴ Niels Bohr International Academy, The Niels Bohr Institute, Blegdamsvej 17, DK-2100, Copenhagen Ø, Denmark

ABSTRACT

Context. The Vertical Shear Instability is one of two known mechanisms potentially active in the so-called dead zones of protoplanetary accretion disks. A recent analysis by Barker and Latter (2015) indicates that a subset of unstable modes shows unbounded growth – both as resolution is increased and when the nominal lid of the atmosphere is extended. This trend possibly indicates a certain level of ill-posedness in previous attempts of linear analysis.

Aims. This research note examines both the energy content of the aforementioned modes and questions the legitimacy of assuming separable solutions for a problem whose linear operator is fundamentally inseparable.

Methods. The reduced equations governing the instability are revisited and the generated solutions are examined using both the previously assumed separable forms and an improved non-separable solution form that is herewith introduced.

Results. Reconsidering the solutions of the reduced equations using the separable form shows that, while the low-order body modes have converged eigenvalues and eigenfunctions (as both the vertical boundaries of the atmosphere are extended and with increased radial resolution), it is also confirmed that the corresponding high-order body modes and the surface modes do indeed show unbounded growth rates. However, the energy contained in both the higher-order body modes and surface modes diminishes precipitously due to the disk’s Gaussian density profile. Most of the energy of the instability is contained in the low-order modes. An inseparable solution form is introduced which filters out the inconsequential surface modes leaving only body modes (both low- and high-order ones). The analysis predicts a fastest growing mode with a specific radial length scale. The growth rates associated with the fundamental corrugation and breathing modes matches the growth and length scales observed in previous nonlinear studies of the instability.

Conclusions. Linear stability analysis of the vertical shear instability should be done assuming non-separable solutions. It is also concluded that the surface modes are relatively inconsequential because of the little energy they contain, and are artifacts of imposing specific kinematic vertical boundary conditions in isothermal disk models.

Key words. Interstellar and circumstellar matter, protoplanetary disks, instabilities, turbulence, waves, methods: analytical

1. Introduction

The Vertical Shear Instability (VSI) (Urpin 2003, Urpin & Brandenburg 1998, Arlt & Urpin 2004, Nelson et al. 2013, McNally & Pessah, 2014, Stoll and Kley 2015), sometimes known as the Goldreich Schubert Fricke instability (Goldreich & Schubert 1967, Fricke 1968) is a linear instability of axisymmetric inertial modes relying on the vertical shear of the basic near-Keplerian flow state. This instability may be active in non-magnetized parts of protoplanetary accretion disks and is perhaps discernible in their dead zones (Turner et al., 2014). Nelson et al. (2013, NGU13 hereafter) and Stoll and Kley (2014) have demonstrated that the instability can generate a modest amount of turbulence, with effective disk α ranging somewhere between 4×10^{-4} up to 10^{-3} . In both studies, the basic background setting is that of a locally isothermal disk with a radial temperature gradient arising either from some external im-

position (NGU13) or naturally manifesting itself due to the inclusion of radiative transfer effects (Stoll and Kley, 2014).

A satisfactory linear stability analysis is still lacking for the disk setting. While the basic essence of the instability has been sketched out using a local point analysis (Goldreich & Schubert 1967, Fricke 1968, Urpin 2003), the way the instability manifests itself in a global or semi-global disk setting is difficult to assess because the basic linear stability problem is non-separable even in the simplest model reduction (NGU13, Barker & Latter 2015, BL15 hereafter). NGU13 and BL15 present such a linear stability analysis using a reduced model set and they show that while the low-order modes that go unstable are consistent with the time scales of the instability seen in the numerical experiments, there are some serious shortcomings associated with the analysis that cast doubt as to whether it provides an accurate description of the physical manifestation of the VSI, especially when analyzed in the locally isothermal disk setting.

Send offprint requests to: O. M. Umurhan
e-mail: orkan.m.umurhan@nasa.gov

The mode analyses done by NGU13 and BL15 show that if one assumes radially propagating traveling waves, there are two classes of modes loosely referred to as *body* modes and *surface* modes. The surface modes come into existence if one imposes no-flow boundary conditions like an impenetrable lid at positions above and below the disk midplane (usually at least a few local disk scale heights or higher). The body modes are present irrespective of the kinematic conditions in the vertical so long as the kinetic energies decay away sufficiently far from the midplane (see below). BL15 also point out that the surface modes become more multitudinous as the radial disturbance wavelengths becomes shorter. BL15 and NGU13 show that for a given value of the radial wavenumber there exists a mode with the fastest growth rate which corresponds, generally, to a surface mode.

However, there are three troubling features:

1. BL15 point out that, as the nominal lid of the atmosphere is extended to infinity, the fastest growing eigenmodes have growth rates that become similarly unbounded as well, growing like \sqrt{m} for integer m representing the number of vertical nodes in the disturbance.
2. BL15 also point out that where no-flow boundary conditions are imposed in the vertical direction, the number of unstable surface modes (with increasingly finer length scales) increases with higher radial resolution, possibly suggesting that the fundamental problem in the VSI setup itself could be ill-posed – at least with respect to these surface modes.
3. As the wavelength of the radially propagating traveling wave becomes larger, similarly the growth rate increases in an unbounded way.

As with regards to the third deficiency, both numerical simulations of NGU13 and Stoll & Kley (2014) indicate that there exists a radial scale of maximum linear growth yet neither of the analyses of the asymptotically reduced equations examined by NGU13 nor BL15 admit such a trend. Is it possible that the reason for this is due to the breakdown in the validity of the reduced equations which hinges on the assumption of radial geostrophy in the dynamics, or might this be a problem with the assumption of radial traveling waves? These are reviewed in more detail in Section 2.

In Section 3, we argue that the first two of the above listed troubling features poses no serious deficiency in either the reduced set of equations or upon the robustness/validity of the VSI itself. This is because both the surface modes and the other high nodal modes (i.e. high m) carry very little of the total vertical kinetic energy of the system. As with regards to the third issue, we consider this pathology to be a shortcoming of assuming a radial traveling wave-like solution and not to be a deficiency of the reduced set of equations. This in turn is related intimately to incorrectly assuming separable solution forms for a problem which is inherently inseparable. We present an improved approximation in Section 4, wherein we adopt a relatively tractable non-separable solution form and reanalyze the reduced equations. We find that there exist maximally growing disturbances at some finite radial length scale and that they, in turn, match the growth rates and fastest growing radial scales reported in NGU13. In Section 5 we briefly discuss our findings.

2. Background

In both NGU13 and BL15, the following asymptotic reduced set of equations governing the dynamics of the VSI was shown to be appropriate in describing the linear development of the instability for axisymmetric disturbances:

$$0 = 2\Omega_0 v - \frac{\partial \tilde{\Pi}}{\partial x}, \quad (1)$$

$$\frac{\partial v}{\partial \tau} = -\frac{1}{2}\Omega_0 \tilde{u} - \frac{\Omega_0}{2} qzw, \quad (2)$$

$$\frac{\partial w}{\partial \tau} = -\frac{\partial \tilde{\Pi}}{\partial z}, \quad (3)$$

$$0 = \frac{\partial u}{\partial x} + \frac{\partial w}{\partial z} - zw. \quad (4)$$

With Ω_0 the local rotation rate of the disk section at a distance R_0 from the parent star, this above set was obtained assuming that the spatial and temporal scales of motion relate according to the following scalings: temporal dynamics are given by $\mathcal{O}(1/\epsilon\Omega_0)$, radial dynamic scales x are $\mathcal{O}(\epsilon^2 R_0)$, and the vertical scales z are on the scale height $H_0 = \mathcal{O}(\epsilon R_0)$ in which the small parameter $\epsilon \equiv H_0/R_0$ measures the relative thinness of the disk (which is usually taken to be approximately 0.05 in most theoretical studies including the ones cited above). The scaled radial and vertical velocities are u and w , respectively, while v is the deviation azimuthal velocity with respect to the background near-Keplerian flow, and $\tilde{\Pi}$ is the scaled pressure perturbation. These equations model disk inertial modes with very short radial wavelengths. The degree of the vertical shear, which varies with disk height z , is controlled by the parameter q (where no vertical shear is equivalent to $q = 0$). In both NGU13 and Stoll & Kley 2014, the value of $q = -1$ is adopted. Equation (1) states that the disturbances are largely in radial geostrophic balance. Equations (2-3) are the azimuthal and vertical momentum equations while equation (4) is the anelastic equation of state. See both NGU13 and BL15 for further details regarding the derivation of this set of reduced equations. Because the equations have been appropriately non-dimensionalized, henceforth we set $\Omega_0 = 1$ on all of the Coriolis and vertical shear terms appearing in equations (1-2).

This simplified model may then be combined into a single PDE for the scaled pressure perturbation

$$-\frac{\partial^2}{\partial t^2} \frac{\partial^2 \tilde{\Pi}}{\partial x^2} + \frac{\partial^2 \tilde{\Pi}}{\partial z^2} + \left(1 + q \frac{\partial}{\partial x}\right) z \frac{\partial \tilde{\Pi}}{\partial z} = 0. \quad (5)$$

Assuming normal mode solutions $\tilde{\Pi} = \hat{\Pi}(x, z) e^{-i\omega t} + \text{c.c.}$ turns the above PDE into the simpler one:

$$\omega^2 \frac{\partial^2 \tilde{\Pi}}{\partial x^2} + \frac{\partial^2 \tilde{\Pi}}{\partial z^2} + \left(1 + q \frac{\partial}{\partial x}\right) z \frac{\partial \tilde{\Pi}}{\partial z} = 0. \quad (6)$$

The problem remains then to construct solutions of this system and determine the eigenvalue ω determining the temporal response. Inspection of the above form shows that this system is inseparable when $q \neq 0$ - which introduces a number of issues with regards to linear stability analyses which we discuss briefly below.

One might proceed analyzing this system assuming an approximate separable form.¹ For instance, as was done by BL15, one can consider the relatively tractable traveling-wave ansatz

$$\hat{\Pi} = Z(z)e^{ikx}. \quad (7)$$

Then equation (6) simplifies further to

$$-k^2\omega^2 Z + \frac{\partial^2 Z}{\partial z^2} + (1 + iqk)z \frac{\partial Z}{\partial z} = 0, \quad (8)$$

where $Z(z)$ is an, as yet undetermined, vertical structure function. The above equation, which is explicitly the same form as appearing in BL15, is in the form of Hermite's equation. One solution of this system that admits tractable analytic results is to allow perturbations to show (at most) algebraic growth as $|z| \rightarrow \infty$, in which case

$$Z(z) = He_m(z) \quad (9)$$

is an acceptable solution where m is a positive index and He_m is the Hermite polynomial of order m . The index m counts the number of vertical nodes in the pressure eigenfunction, and so it is referred to as indicating this quality throughout the rest of this research note. When inserted into equation (6), we find that this solution form is an actual solution provided the following relationship holds:

$$\omega = \frac{\sqrt{m}}{k} \sqrt{1 + ikq}. \quad (10)$$

As discussed in BL15, the growth rate associated with this form increases without bound as $k \rightarrow 0$. We agree that this is pathological for a number of reasons, the following two being most prominent: (i) the approximation of radial geostrophy most likely breaks down when the horizontal wavelengths become large, and (ii) because, as we show in the next section, the traveling wave ansatz is also deeply flawed. This solution is also problematic because the growth rates also grow without bound both as the integer m becomes large and as k becomes small. Nonetheless, this simplest solution indicates that the system is ill-posed as higher-order vertical modes (increased m) are included in the analysis.

Note that this solution ansatz cannot recover surface modes for the obvious reason that no kinematic boundary conditions are either emplaced or enforced in the vertical. We also note that since both the atmosphere density drops off as a Gaussian (i.e. $\rho_0 \sim \exp -z^2/2$) and that eigenmodes have z^m structure, the effect of adopting a free vertical boundary condition is really to say that kinetic energies of all modes decay to zero as $z \rightarrow \pm\infty$.

Another approach is the one taken by NGU13 and BL15 in which equation (8) is solved with no-normal flow boundary conditions at the vertical boundaries at $z = \pm H$ (note

¹ If the calculation domain is on a uniform rectangular grid, a sure way to guarantee an unambiguous determination of eigenvalues and eigenmodes is to apply a finite difference discretisation of equation (6). With N_z and N_x discretisation points in the vertical direction and radial direction, then the resulting eigenvalue system requires inversion of $(N_x N_z) \times (N_x N_z)$ sized (relatively) sparse matrices. High resolution in both the radial and vertical direction are desirable and therefore $N_z \approx 150$, $N_x \approx 100$ which means constructing matrices that are prohibitively large to invert or, equally speaking, challenging to reconfigure into known sparse matrix formulations.

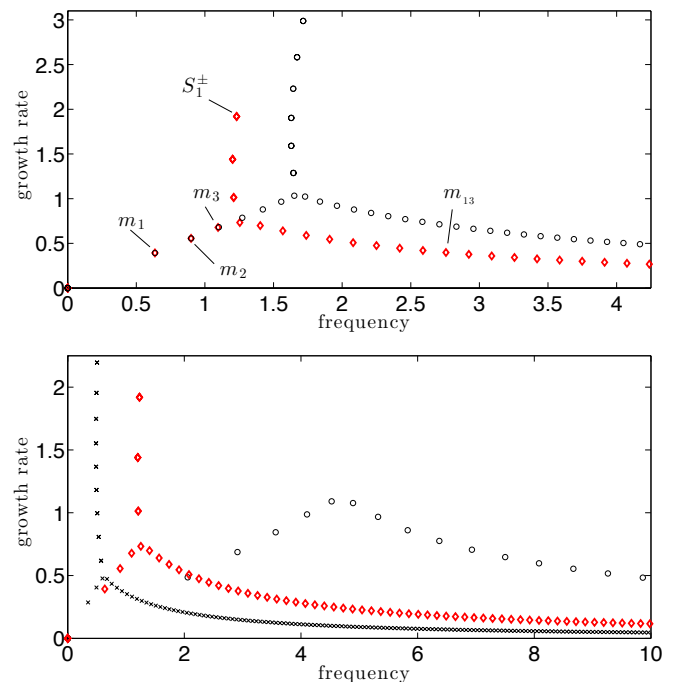


Fig. 1: The growth rates, $\text{Im}(\omega)$, and frequencies, $\text{Re}(\omega)$, of solutions of equation (8) subject to no-normal flow boundary conditions at $z = \pm H$, where H is in units of scale heights. *Top panel*: Distribution shown for $k = 2$ and $H = 5$ (diamonds) and $H = 7$ (open circles). As H increases more surface modes become activated and high-order body modes have larger growth rates. In both cases shown, the frequency and growth rates of low-order body modes (labeled m_1, m_2, m_3) remain unchanged. Note that the surface modes generally appear in pairs as indicated by superscript labeling the topmost surface mode S_1^\pm . This panel confirms the trends reported by BL15. *Bottom panel*: Distribution of the complex frequencies shown for differing values of k with fixed $H = 5$: $k = 5$ (crosses), $k = 2$ (diamonds), $k = 0.5$ (open circles). The growth rates increase without bound as k is decreased, with the same trend found in the problem with no vertical boundaries as found in expression (10). Note that as k is increased, the number of surface modes increases including the maximum growth rates - also confirming the results reported in BL15.

that H refers to the height of the solution domain and H_0 refers to the disk scale height in this paper), which amounts to imposing that $\partial_z \tilde{\Pi} = 0$ there provided $\omega \neq 0$, which follows from the normal mode form of equation (3). The general solution of (8) is given by

$$Z(z) = A He_\lambda(z) + B {}_1F_1 \left(-\frac{\lambda}{2}, \frac{1}{2}, \frac{z^2(1 + iqk)}{2} \right)$$

where ${}_1F_1$ is confluent hypergeometric function of the first kind and where λ is the usual separation constant which is determined through the application of boundary conditions. The second of these special functions do not offer very much in the form of analytic ease or insight (NGU13) except in the guise of certain asymptotic limits (BL15) and, as such, it is more convenient to solve equation (8) directly numerically.

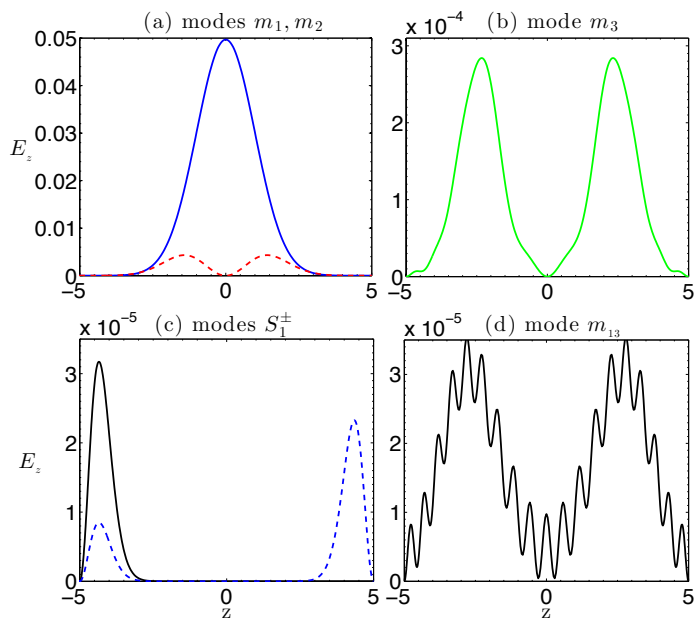


Fig. 2: Vertical kinetic energy density plots E_z plotted for the modes labeled in the top panel of Fig. 1 corresponding to solutions of (8) with $H = 5$ and $k = 2$. Each corresponding vertical velocity eigenfunction w is normalized such that $\int_{-5}^5 |w| dz = 1$. (a) low-order body modes m_1, m_2 (solid and dashed lines respectively), (b) low-order body mode m_3 , (c) fastest growing surface modes S_1^+, S_1^- (solid and dashed lines respectively) and (d) a high-order body mode m_{13} . The lowest order body mode m_1 is the fundamental corrugation mode and dominates the energy density contained in the high-order body modes and the surface modes by at least a factor of 10^3 . The energy density contained in the fundamental breathing mode (m_2) is a factor 10 less than the mode m_1 .

The numerical eigenvalues determined by this procedure recover the surface modes as well as the body modes of the VSI. The low-order body modes (the fundamental and first overtone breathing and corrugation modes) are also recovered with eigenvalues consistent with the numerical results of NGU13. However this system introduces apparent pathologies which are depicted in Figure 1. There are generally three branches of solutions: one associated with low-order body modes with relatively low frequencies, another branch of body modes with higher frequencies and a third stem consisting of surface modes. The high frequency branch of body modes show decreasing growth rates as the mode frequency increases while the low-order body modes show increasing growth rate with increasing frequency.

However, as BL15 demonstrate, when the location of the vertical height is increased, it is found that (a) the growth rates of the high frequency branch increase (b) the growth rates of the surface body modes also increase while (c) the growth rates and frequencies of the low-order body modes remain unchanged and (d) as the lid of the atmosphere is raised to $\pm\infty$ the low- and high-order body modes line up with the frequencies and growth rates found expressed in equation (10), that is, the response predicted assuming the ansatz found in equation (7). While it would seem that imposing vertical no-flow boundary conditions lifts the

ill-posedness due to the unbounded growth rates with respect to m in the body modes arising from the ansatz in equation (7), the problem comes back as $H \rightarrow \infty$ since the growth rates in the high-order body modes and surface modes correspondingly increase, seemingly without bound. This is problematic and indicates that the problem may be ill-posed after all.

The situation becomes even worse when considering the behavior of the surface modes, as BL15 indicate: increasing the radial resolution (larger k) proliferates the number of surface modes attached to the upper and lower no-flow boundaries as the second panel of Figure 1 clearly illustrates. Raising the value of the lid also increases the growth rate of the fastest growing modes also indicating some kind of ill-posedness due to the surface modes as well.

Moreover, another serious shortcoming implied by the results of the linear stability solutions developed in NGU13 and BL15 is that they do not predict finite, non-zero maximally growing radial wave disturbances – something that is however observed in the numerical experiments of NGU13 and Stoll & Kley (2014). This suggests that assuming wave-like modes in the radial direction is flawed.

3. Mode kinetic energies

In spite of these troublesome features, these approximate theoretical solutions reveal much about the physical nature of the developing instability – especially with regards to the high frequency body modes and the proliferating surface modes. For example, they indicate something about the relative energy content for each mode. The low-order body modes carry most of the inertia of the disk disturbances as their amplitudes are greatest near $z = 0$ (NGU13, BL15). Since these are also locations where most of the disk mass is concentrated, the energy contained in these low-order body modes dominate the corresponding energy contained in the higher-order body and surface modes. This has direct consequence with regards to the interpretation of the VSI, even in the framework of this somewhat incomplete analysis.

To quantitatively illustrate this, we show in Figure 2 a comparison of the relative energy densities contained in representative modes labeled in the top panel of Figure 1, corresponding to solutions of (8) with $H = 5$ and $k = 2$. From equation (3) it follows that each eigenmode $Z(z)$ generates a corresponding vertical velocity eigenfunction $w = i\omega^{-1}\partial_z Z$. We normalize each such vertical velocity eigenfunction so that

$$\int_{-H}^H |w| dz = 1. \quad (11)$$

Since the reduced equations represent an isothermal atmosphere, the steady-state density is given by $\rho_0 = \exp(-z^2/2)$. We also recall that this instability is one in which the perturbation vertical kinetic energy density dominates over the radial and azimuthal kinetic energy densities (NGU13, Stoll & Kley, 2014). As such, we consider the vertical kinetic energy density E_z of each of the corresponding modes defined by $E_z(z) \equiv 0.5\rho_0|w|^2$. The mode labeled ‘ m_1 ’ is the fundamental corrugation mode (FCM) while the mode labeled ‘ m_2 ’ is the fundamental breathing mode (FBM) so that, for example, the expression $E_z(z, m_1)$ corresponds to the energy density of the FCM, and so on. We also define for each mode a total vertically integrated density

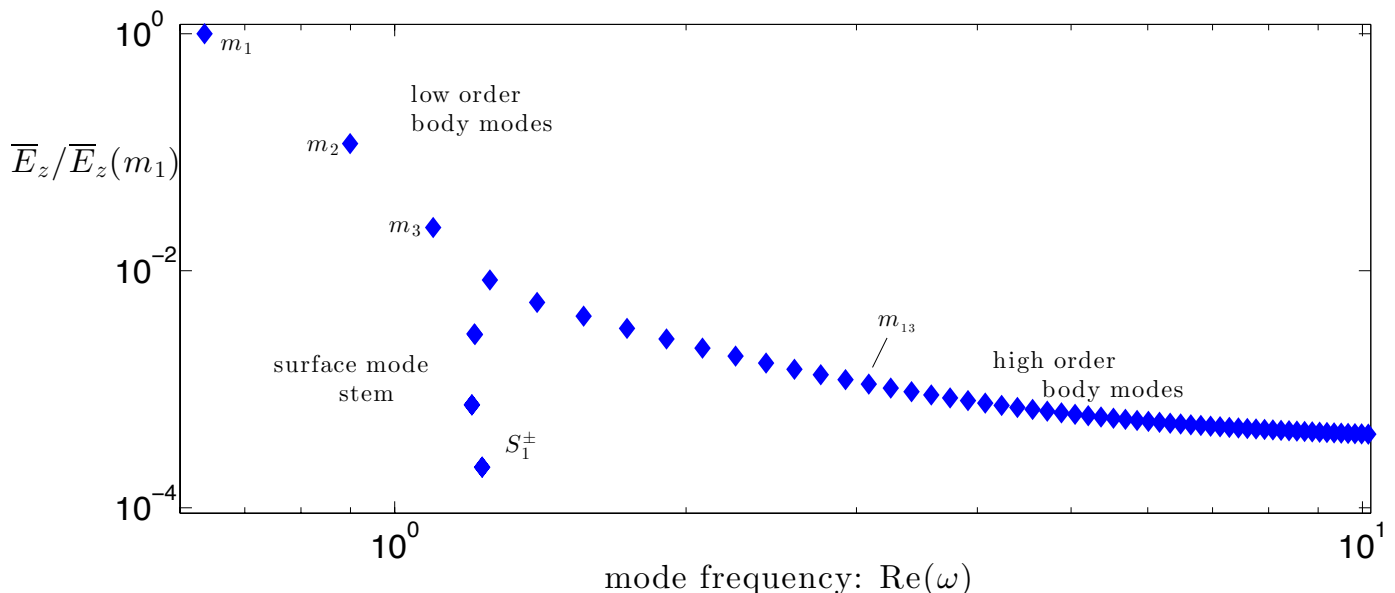


Fig. 3: Total vertically integrated vertical kinetic energies \bar{E}_z as a function of mode frequencies, $\text{Re}(\omega)$, corresponding to solutions of (8) with $H = 5$ and $k = 2$. \bar{E}_z is plotted normalized to the corresponding vertically integrated energy of the fundamental corrugation mode, i.e. $\bar{E}_z(m_1)$. Note the relative weakness in the power of the surface modes located in the frequency window 1.2 and 1.3. The labeled modes displayed in Figure 2 are labeled here as well.

$\bar{E}_z \equiv \int_H^H 0.5\rho_0|w|^2 dz$ (i.e. a surface energy density). When we refer to the surface energy density of a particular mode we write, for example $\bar{E}_z(m_1)$, to indicate the surface energy density of the FCM, and so on.

Figure 2 plots the energy densities \bar{E}_z for the various modes admitted by the system with parameter values $k = 2, H = 5$, wherein each vertical velocity normal mode is normalized according to (11). We see that the relative energy density content is greatest with FCM and dominates the FBM by a factor of 10. The energy density distribution in the other higher-order body modes are reduced by at least a factor of 100 compared to the FCM. The energy density contained in the two fastest growing surface modes is diminished by a factor of 1000 compared to the FCM.

A comparison of the total vertically integrated energies in these various modes emphasizes further the relative unimportance of the high-order body and surface modes. Expressing this quantity relative to the vertically integrated energy density of the FCM ($\bar{E}_z(m_1)$), we have for the selected modes: for the FBM, $\bar{E}_z(m_2) \approx 0.11\bar{E}_z(m_1)$; for the first overtone corrugation mode, $\bar{E}_z(m_3) \approx 8.3 \times 10^{-3}\bar{E}_z(m_1)$; the selected high-order body mode m_{13} : $\bar{E}_z(m_{13}) \approx 1.3 \times 10^{-3}\bar{E}_z(m_1)$; and for the two surface body modes, both of which have the same amount of vertically integrated energy contained within, $\bar{E}_z(S_1^\pm) \approx 2.2 \times 10^{-4}\bar{E}_z(m_1)$. These trends are plotted in Figure 3 together with the first 50 vertical eigenmodes, which shows demonstrably that the energy contained in the modes drops with increased values of m . We similarly plot the relative vertically integrated kinetic energy densities for models where $H = 7, k = 2$ (Figure 4) and $H = 8, k = 5$ (Figure 5) and we see how increasing the resolution (going to larger k) and extending the atmosphere lid shows how the low-order modes get increasingly populated (as BL15 point out) and

that the \bar{E}_z energies contained in the corresponding surface and high-order body modes get even further diminished.

Most importantly we confirm the trend reported by BL15 in which the energy in the low order body modes remains steady as H is increased - this is especially true for the FCM and FBM but also becomes a characteristic feature of increasing overtones as H is taken larger. In reference to Figure 3 all the body modes to the left of the triple junction where the surface mode stem branch meets the low order and high order body modes have energies that are unchanged as H is increased. Increasing H however moves the location of the triple junction toward higher order body modes but the energies of the low order body modes (i.e. those left of the triple junction) do not change with increased H .

The weak relative energy carrying potential of both the high order body modes and the branch of surface modes comes about because while the high order body modes and surface modes have have strong power in the vertical velocity field for large values of $|z|$, the corresponding kinetic energy associated with them gets severely diminished because of the Gaussian drop-off associated with the mean density field ρ_0 .

4. An improved approximate solution

While we cannot address all of the concerns enumerated in Section 2, we offer an improved solution ansatz to the eigenvalue problem posed by equation (6). The simulations presented in NGU13 and Stoll & Kley (2014) employ a numerical set-up in which radial boundaries are enforced. Such boundaries introduce effects that alter the growth rates and character of the low-frequency body modes - the very modes observed to carry the instability into the nonlinear regime. We demonstrate here that the unbounded growth

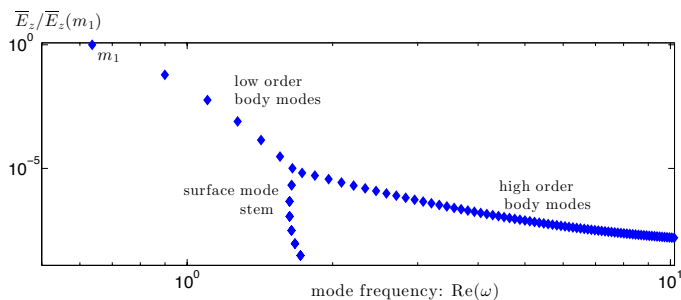


Fig. 4: Like Figure 3 except with $H = 7$. The power contained both in the surface and high-order body modes is diminished as the atmosphere lid is set further away. Note that the energy in the low order body modes remain unchanged, especially the FCM and FBM. The only difference is that an increasing number of body modes appear and remain stable with increased values of H .

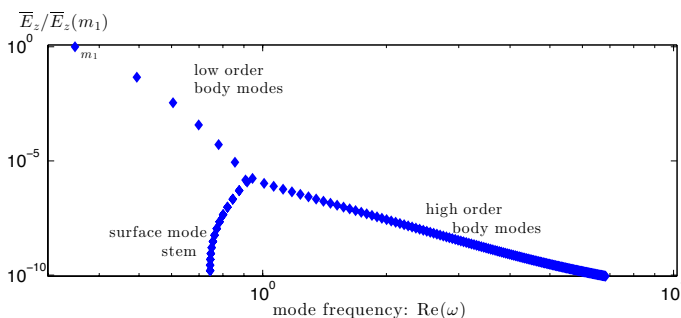


Fig. 5: Like Figure 3 except with $H = 8$ and $k = 5$. Note the diminished energy carrying capacity of both the surface modes and the high-order body modes as both the lid of the atmosphere is made larger and higher radial resolution modes are considered. The energy of the low order body modes, especially the FCM, FBM and the first overtone corrugation mode remain unchanged compared to their energies for smaller values of H depicted in the two previous figures.

predicted by assuming wavelike disturbances in the radial direction is an artifact of assuming radially-traveling wave solutions and that this pathology is removed by the imposition of some kind of fixed boundary condition. Furthermore, the imposition of boundary conditions selects a fastest growing radial wavenumber that matches the growth rates found in the aforementioned numerical experiments.

In order to represent the effect of radial boundaries, the following non-separable ansatz is assumed:

$$\hat{\Pi} = P_m(z, x) = \sum_{n=0}^m P_{n,m}(x)z^n. \quad (12)$$

for m a positive integer and a set of unknown functions of x , $P_{n,m}(x)$.² This solution form is one borrowed from singular value decomposition methods and has been used in other disk studies (e.g. Lubow & Pringle 1983). We note already

² This ansatz form is non-separable for all integer values of $m \geq 2$, and is separable only for the $m = 1$ mode.

that the ansatz found in equation (12) builds into the solutions unbounded algebraic spatial growth as $|z| \rightarrow \infty$ and will predict the same kind of unbounded growth in which $\text{Im}(\omega) \sim \sqrt{m}$, just as the simple solution shown in equation (10). But as we already noted in Section 2, this means these solutions are ones in which the kinetic energies always decay as $z \rightarrow \pm\infty$. On the positive side, these solutions are not burdened by the introduction of surface modes.

As such, we adopt this solution form and insert it into equation (6). Separating out like orders in powers of z turns this system into $\mathcal{O}(\frac{m+1}{2})$ nested ODEs for the unknown functions $P_{n,m}$. For $n = m$ we have the “top” equation

$$\omega^2 \frac{\partial^2 P_{m,m}}{\partial x^2} + m \left(P_{m,m} + q \frac{\partial P_{m,m}}{\partial x} \right) = 0, \quad (13)$$

while for $0 \leq n < m$ we have the remaining “slaved” equations

$$\omega^2 \frac{\partial^2 P_{n,m}}{\partial x^2} + n \left(P_{n,m} + q \frac{\partial P_{n,m}}{\partial x} \right) = -(n+2)(n+1)P_{n+2,m}. \quad (14)$$

The above system has even and odd symmetries associated with it, so that there are so-called breathing modes (even m) and corrugation modes (odd m). The fundamental corrugation mode (FCM) corresponds to $m = 1$ while the fundamental breathing mode (FBM) is associated with $m = 2$.

For this particular demonstration, we assume no normal flow boundary conditions at some inner and outer radial position, i.e. $u = 0$ at $x = \pm L_x$, where $L_x > 0$. In terms of the variables we use, the expression of this condition is found by rewriting equation (2) in terms of the normal mode ansatz

$$-i\omega \frac{\partial \tilde{\Pi}}{\partial x} + \frac{qz}{i\omega} \frac{\partial \tilde{\Pi}}{\partial z} = 0. \quad (15)$$

Given the solution form (12) and since z^n are linearly independent with respect to one another for integer n , each function $P_{n,m}$ must separately satisfy

$$\frac{\partial P_{n,m}}{\partial x} + \frac{qn}{\omega^2} P_{n,m} = 0 \quad (\text{at } x = \pm L_x). \quad (16)$$

The solution method for the full problem is now straightforward: (i) solve the “top” equation (13) subject to boundary conditions and then (ii) solve the “slaved” equations (14) subject to the boundary conditions expressed in equation (16) for each $P_{n,m}$ for decreasing values of n (by 2) until one terminates either at $n = 0$ (breathing modes) or $n = 1$ (corrugation modes). A detailed depiction of the full solution will be left for a future study. Of concern to us here, however, is the fact that the top equation yields the eigenvalue ω . In fact, it is straightforward to show that

$$P_{m,m} = \left(A_j \sin k_j x + B_j \cos k_j x \right) \exp \left(-\frac{qm}{2\omega^2} x \right), \quad (17)$$

is a solution to equation (13) provided $\omega = \omega(k_j)$ satisfies

$$\frac{\omega^2}{m} = \frac{1 \pm \sqrt{1 - k_j^2 q^2}}{2k_j^2}, \quad (18)$$

together with $k = k_j \equiv j\pi/2L_x$, where j is any integer including zero. When j is an odd integer then $A_j = k_j$, $B_j =$

$-qm/2\omega^2$ while when j is an even integer (including zero) $A_j = -qm/2\omega^2$, $B_j = -k_j$.

Since all the k_j are real and their multitude are controlled by L_x , we can consider the set of k_j as part of a continuum of real values given as k and we can analyze these results accordingly. It follows that unstable solutions exist only if $|kq| > 1$, and after a little algebra it implies that the growth/decay rate is given by

$$\text{Im}(\omega) = \pm \sqrt{m} \frac{\sqrt{|kq| - 1}}{2k}. \quad (19)$$

This solution says that there is a wavelength of maximal growth k_{max} and corresponding growth rate σ_{max} which are given by

$$|k_{\text{max}}| = \frac{2}{|q|}, \quad \sigma_{\text{max}} = \sqrt{m} \frac{|q|}{4}. \quad (20)$$

Restoring these results in terms of the physical scalings of the disk, this implies a maximally growing wavelength Λ_{max} and growth rate Σ_{max} expressed as

$$\begin{aligned} \Lambda_{\text{max}} &= \pi \epsilon^2 |q| R_0 = \pi |q| \frac{H_0^2}{R_0}, \\ \Sigma_{\text{max}} &= \epsilon \sqrt{m} \frac{|q|}{4} \Omega_0 = \sqrt{m} \frac{|q|}{4} \frac{H_0}{R_0} \Omega_0, \end{aligned} \quad (21)$$

the latter of which, in terms of local disk orbit times ($\text{orb} = 2\pi/\Omega_0$), is given as $\Sigma_{\text{max}} = 0.5\epsilon\sqrt{m}|q|\pi \text{orb}^{-1}$.

5. Discussion

The solution developed in Section 4 is an improvement over the previous ones reported in the literature (namely NGU13 and BL15). We enumerate below some relevant observations regarding it.

1. In the numerical experiments reported in NGU13, it was shown that in model disks where $\epsilon = 0.05$, and $q = -1$, the growth rate of the perturbation kinetic energy during the early phase (between 10-25 orbits of the inner disk) of the growing VSI is about 0.25orb^{-1} (see the right panel of their Figure 1.) Inspection of the dynamical response during this same phase (see their Figure 3) shows primarily a breathing mode character in the vertical velocity. The radial wavelength of the response near the left boundary indicates a size of about $0.009R_0$ (note that this corresponds to approximately 17 grid points resolving the fastest growing radial mode). According to the theory developed in the previous section, the radial scale and growth rate of the fundamental breathing mode (FBM, $m = 2$) is given by equation (21) predicting $\Lambda_{\text{max}} \approx 0.0079R_0$ together with $\Sigma_{\text{max}} \approx 0.11 \text{orb}^{-1}$. However, the growth rate in the kinetic energy is equal to $2\Sigma_{\text{max}} \approx 0.22\text{orb}^{-1}$. These predictions based on this improved approximation compares favorably with the results of the numerical simulations.
2. Similarly, for later times in the simulations reported in NGU13, the growth rate of the simulations after about 25 orbit times show slower growth and the corresponding figures indicate that in this latter phase the disk response is primarily that of the FCM. For the FCM with k as given, the theory predicts a growth rate in the kinetic energy of about $2\Sigma_{\text{max}} (m = 1) \approx 0.15\text{orb}^{-1}$ which approximately matches the slowing seen in the kinetic energy growth rates displayed in Figure 1 of NGU13.
3. The analysis developed using the solution ansatz in equation (12) only captures the essence of the low-order body modes and cannot say anything about the surface modes simply because no vertical boundary conditions are applied. However, given our reflections in Section 3 regarding the kinetic energy density content of these modes, the surface modes are likely ephemeral having no significant dynamical effect upon the development of the VSI in the bulk interior where most of the disk inertia is contained.
4. Despite the improved theoretical construction embodied in the ansatz of equation (12), especially with regards to the correct behavior predicted with respect to a fastest growing radial mode, the theory still indicates unbounded growth as the vertical node number m increases. Is this indicative of a profound flaw in the ansatz or might it be a real effect? Given our reflections upon the lack of energy contained in high-order body modes and surface modes (Section 3), it may be that the theoretical predictions are actually valid and that despite the unbounded growth predicted for increasing m , the main instability and turbulent development in non-linear calculations is driven primarily by the fundamental breathing and corrugation modes. *The concomitant fast growing high-order body modes and surface modes likely have little effect upon the overall development of the VSI primarily because they contain so little energy by comparison to the fundamental modes.*
5. Related to the previous point, unless by conspiracy power is initially placed only in high-order modes or in the strongly localized surface modes, we believe that the VSI develops robustly independent of them - even if artificial boundary conditions are emplaced on the upper and lower parts of a numerically modeled disk. We agree with BL15 that adding a bit of artificial viscosity, or possibly a sponge (an artifice commonly used in atmosphere GCMs), should either erase or strongly diminish these modes from a numerical calculation. Recall that in both numerical experiments of NGU13 and Stoll & Kley (2014), the velocity fields are shown as time snapshots as the instability develops and they show a strong initial development in the velocity field near the boundaries due primarily to the fast growth of the surface modes. Yet, the kinetic energy densities contained in those disturbances high up in the atmosphere are diminished by a factor of e^{-12} due to the vanishingly small densities up there. It is hard to imagine that the instability ensuing within the bulk of the disk is dependent upon these surface modes and we view them as inconsequential as far as the long term development of the VSI is concerned, including its aggregate turbulent transport. This can be verified by new numerical experiments in which, for instance, one may replace the upper hard boundary by a sponge or something similar.
6. The results of the previous section shows that enforcing boundary conditions at the inner and outer radial positions controls the growth of the VSI and selects for a fastest growing radial structure. As such, we see the

unbounded growth rates resulting from the radial traveling wave ansatz (detailed in Section 2) to be due to the ansatz itself being incorrect and less to be because of a breakdown in the validity of the assumptions undergirding the equation set (1)–(4), namely, the approximation of radial geostrophy of equation (1).

This last point naturally begets the following question: what are the appropriate boundary conditions to use in such disk models? How robust is the VSI to differing radial boundary conditions and how do these attest to the true conditions of protoplanetary disk dead zones?

References

- Arlt R., Urpin V., 2004, *A&A*, 426, 755
Barker A.L., Latter H. N., 2015 (BL15), *MNRAS* (in press)
Fricke K., 1968, *Z. Astrophys.*, 68, 317
Goldreich P., Schubert G., 1967, *ApJ*, 150, 571
Lubow S. H., Pringle J. E., 1993, *ApJ*, 409, 360
McNally, C. P., & Pessah, M. 2014, ArXiv e-prints
Nelson R. P., Gressel O., Umurhan O. M. (NGU13), 2013, *MNRAS*, 435, 2610
Stoll M. H. R., Kley W., 2014, *A&A*, 572, A77
Turner, N. J., Fromang, S., Gammie, C., Klahr, H., Lesur, G., Wardle, M. & Bai, X.N. 2014, *Protostars and Planets VI*, 411-432
Urpin V., Brandenburg A., 1998, *MNRAS*, 294, 399
Urpin V., 2003, *A&A*, 404, 397